Original Article

Correlation of residual stress, hardness and surface roughness with crack initiation and fatigue strength of surface treated additive manufactured AlSi10Mg: Experimental and machine learning approaches

Erfan Maleki, Sara Bagherifard[*], *Mario Guagliano*

Department of Mechanical Engineering, Politecnico di Milano, Milano, Italy

ARTICLE INFO

ABSTRACT

Post-processing methods are widely used to address the issues caused by surface imperfections and bulk defects in additive manufactured materials. In our previous studies, we analysed the effects of different peening-based treatments of shot peening (SP), severe vibratory peening (SVP) and laser shock peening (LSP) on fatigue performance of V-notched laser powder bed fusion AlSi1Mg samples. Herein, the fracture surfaces of failed samples were further analyzed and obtained experimental data were further elaborated by machine learning (ML)-based approach to identify the correlation between residual stress, hardness and surface roughness (all affected by the applied post-treatments) with the depth of crack initiation site and fatigue life of the post-treated samples. ML-based model was developed via a six layer deep neural network (DNN) as well as using stacked auto-encoder (SAE) for pre-training of the used data set. Taking the advantages of SAE, the accuracies of more than 0.96 were obtained for the predicted results. Correlations were obtained by performing parametric analyses and the importance of each input factor was assessed through sensitivity analyses. The obtained results revealed that by enhancing surface hardening and inducing higher compressive residual stresses as well as more efficient surface roughness reduction, deeper crack initiation site and superior fatigue life can be obtained. In addition, it was found that the depth of sub-surface crack initiation had direct relation with fatigue life improvement in the samples.

1. Introduction

As-built additive manufactured (AM) materials exhibit inhomogeneous microstructures [1], multiple forms of porosity [2,3], tensile residual stresses (TRS) [4,5], surface imperfections and high surface roughness [6—10]. These defects affect the performance of LPBF materials, especially in terms of fatigue behavior [11—13]. Many impact-based surface treatments have been suggested for addressing surface imperfections as non-subtractive post-treatments for AM materials, such as shot peening (SP) [14,15], ultrasonic shot peening (USP) [16],

severe vibratory peening (SVP) [17], cavitation peening (CP) [18,19], ultrasonic peening (UP) [20], laser shock peening (LSP) [21—24] and ultrasonic nanocrystal surface modification (UNSM) [25—27]. These have been proved to efficiently remove the surface irregularities and homogenize the surface morphology of AM materials. Moreover, these treatments have a high potential in inducing surface layer grain refinement, surface hardening and generating high compressive residual stresses (CRS) leading to notable fatigue behavior improvement [28—31]. In addition, it should be noted that other category of post-processing methods such as heat treatments (HT) have been be applied on AM materials for improved fatigue behavior [32—34]. HT can homogenize the microstructure and release the unfavourable tensile residual stresses of the as-built condition caused by the complex thermal history during melting and solidification stages [35].

On the other hand, machine learning (ML) methods such as neural networks (NNs) have gained considerable attention recently, due to their efficiency in comprehensive modelling of complex phenomena in various fields of science and engineering [36—41]. As one of the latest generations of NNs, deep neural networks (DNNs) with multiple layers exhibit high performance in modelling of non-linear systems. Taking advantage of deep learning methods such as restricted Boltzmann machine (RBM) and deep belief network (DBN) [42,43], it is feasible to develop DNN using greedy layer-wised methods with pre-training even with a small experimental data set. Also, specific techniques for pre-training of DNN such as stacked auto-encoder (SAE) are presented to make the development of DNN possible with even smaller data set but high accuracy [44—47].

ML-based approaches have been used in the filed of AM, in particular, for fatigue behavior prediction of laser powder bed fusion (LBPF) materials [48—52].

In this study, first, the experimental data from our previous studies were gathered to compare the effects of different peening-based treatments of shot peening [53], severe vibratory peening [17] and laser shock peening [54] on crack initiation and fatigue behavior of V-notched LPBF AlSi1Mg samples. These experimental results were used for developing a ML-based model with deep learning approach. The ML-based approaches were used for the determination of the correlation between mechanical and physical parameters with the depth of crack initiation site and fatigue life of post-processed samples. Microhardness and residual stresses were continuously mapped on the fracture surface to obtain the corresponding values at crack initiation site. The distribution of applied stresses on the notch root section was estimated by an elastic finite element model.

Then different NNs including shallow neural networks (SNNs), which have 1 or 2 hidden layers and deep neural networks (DNNs), which have more than 2 hidden layers, as well as SAE assigned DNN (SADNN) were developed. In the first model, superimposed stresses through the notch section, hardening index and surface roughness were considered as inputs and the depth of crack initiation site, the relative height of fracture plane and fatigue life were gathered as output parameters. Another model was developed to analyze the effect of depth of crack initiation site and the relative height of fracture plane on fatigue life. SAE was used for pre-taring of the data fed to the two DNN models. The experimental data were fed to the constructed models for obtaining the correlation between residual stress, hardness and surface roughness with the depth of crack initiation site and fatigue behavior of V-notched LPBF AlSi10Mg samples subjected to different peening treatments.

2. Experimental procedures

Fig. 1a shows a schematic representation of the manufacturing process for the V-notched LPBF samples with three distinct regions of upward face, notch root and downward face; the
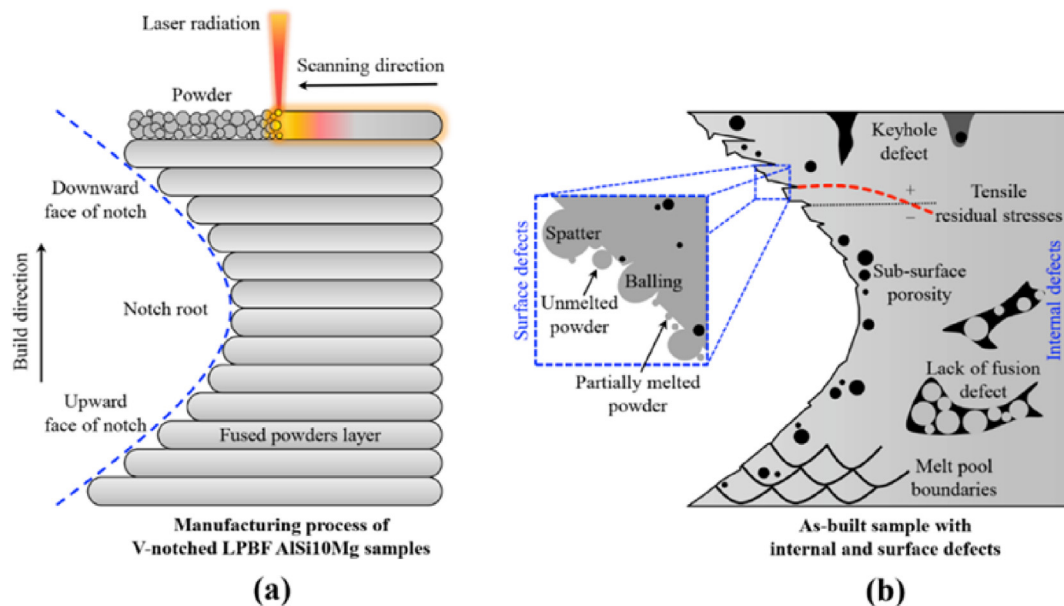

Fig. 1 — Schematic illustration of (a) the manufacturing process of V-notched LPBF AlSi10Mg samples and (b) the corresponding internal and surface defects.

Table 1 – Parameters of the applied post-treatments [17,53,54].

SP treatment	Shot material	Shot hardness (HRC)	Shot standard	Shot diameter (mm)	Almen intensity (A 0.001 inch)	Surface coverage (%)
SP1	Cast steel	48–50	S 170	0.43	10	100
SP2	Ceramic	60–62	Z 100	0.1–0.15	5	100

SVP treatment	Shot material	Shot hardness (HRC)	Frequency (Hz)	Shot type	Shot diameter (mm)	Peening duration (min)
SVP1	Steel	52	50	100Cr6	1	15
SVP2	Steel	52	50	100Cr6	1	30

LSP treatment	Frequency (Hz)	Pulse duration (ns)	Laser source wavelength (nm)	Pulse overlapping (%)	Laser beam energy (J)	Laser energy density (GW/cm²)
LSP1	10	10	1064	50	1.5	3
LSP2	10	10	1064	50	4.5	9

internal and surface defects corresponding to these three zones are shown in Fig. 1b. In our previous study, we applied three different post-processing methods of SP [53], SVP [17] and LSP [54] on the notched samples with parameters mentioned in Table 1. Each surface treatment was applied considering two (low and high) levels of kinetic energy.

To be able to compare the influence of the surface treatments, the kinetic energy levels were kept comparable between the treatments using Almen intensity that is a standard index widely employed in the field of SP. All post-processing methods were applied on Almen strip A and the induced curvature, typically referred to as arc height, were measured to be comparable between the three treatments; the two intensities of 4–6 A and 10–12 A [0.001 inch] were set for the processes with low and high energy, respectively. Schematic illustration of the applied treatments is presented in Fig. 2a–c and the measured arc heights at different exposure times for each treatment is shown in Fig. 2d.

Considering all of the applied post-treatments, 7 different sets of samples including as-built (AB) as control sample and 6 treated sets of AB + SP1, AB + SP2, AB + SVP1, AB + SVP2, AB + ULSP1 and AB + LSP2 samples were considered.

Fig. 3a depicts the shape and size of the fatigue samples with notch root dimeter of R = 1 mm manufactured using gas atomized AlSi10Mg powders with mean diameter of 46.65 μm. The details of the experiments for roughness, microhardness and residual stress measurements are presented in our previous study [53]. In addition, fatigue life of all sets of samples was assessed performing rotating bending fatigue test (stress ratio of R = −1) at a fixed nominal stress amplitude of 110 MPa considering run-out limit of 6×10^6 cycles and a rotational speed of 2500 rpm. Fig. 3b shows a schematic of the fatigue test set-up. Five samples were tested for each condition and the average fatigue lives are reported. Fractography analysis was performed on the broken samples using Zeiss EVO50 scanning electron microscope. The corresponding stress distribution in the minimum cross-section (diameter of 8 μm) of the as-designed geometry was obtained by finite element (FE) simulation considering the load applied in the experiments, as represented in Fig. 3c. A linear elastic FE model was developed by commercial software of Abaqus/Explicit 2019 using C38DR elements (8-node linear brick) considering a cylindrical geometry with the diameter and notch geometry of the real sample, to obtain the stress distribution through the minimum cross-section. The FE results demonstrate the classic distribution of axial stresses under bending with the highest stress concentration occurring at the notch root, as expected. Based on the performed measurements, the diameter of the minimum cross-section did not significantly vary between the as-designed, as-built and surface-treated samples (about maximum 0.1 mm), the distribution of the axial stresses obtained from the FE analysis was considered valid in all cases.

3. Implementation of machine learning

ML was used for analyzing the correlation between residual stress, hardness and surface roughness with crack initiation site and fatigue life of the post-treated notched LPBF AlSi10Mg samples. Firstly, a ML-based model using SNN was developed
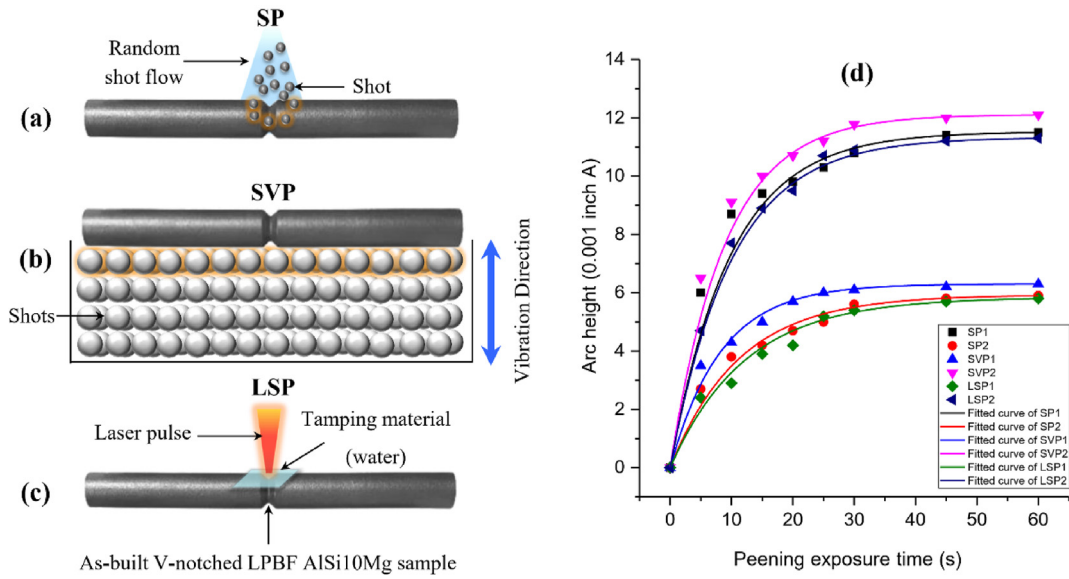
Fig. 2 − Schematic illustration of the applied post-processing methods of (a) SP, (b) SVP and (c) LSP; (d) the measured arc heights at different exposure times for all the considered post-treatments resulting in two ranges of Almen intensity of 4−6 A and 10−12 A [0.001 inch].
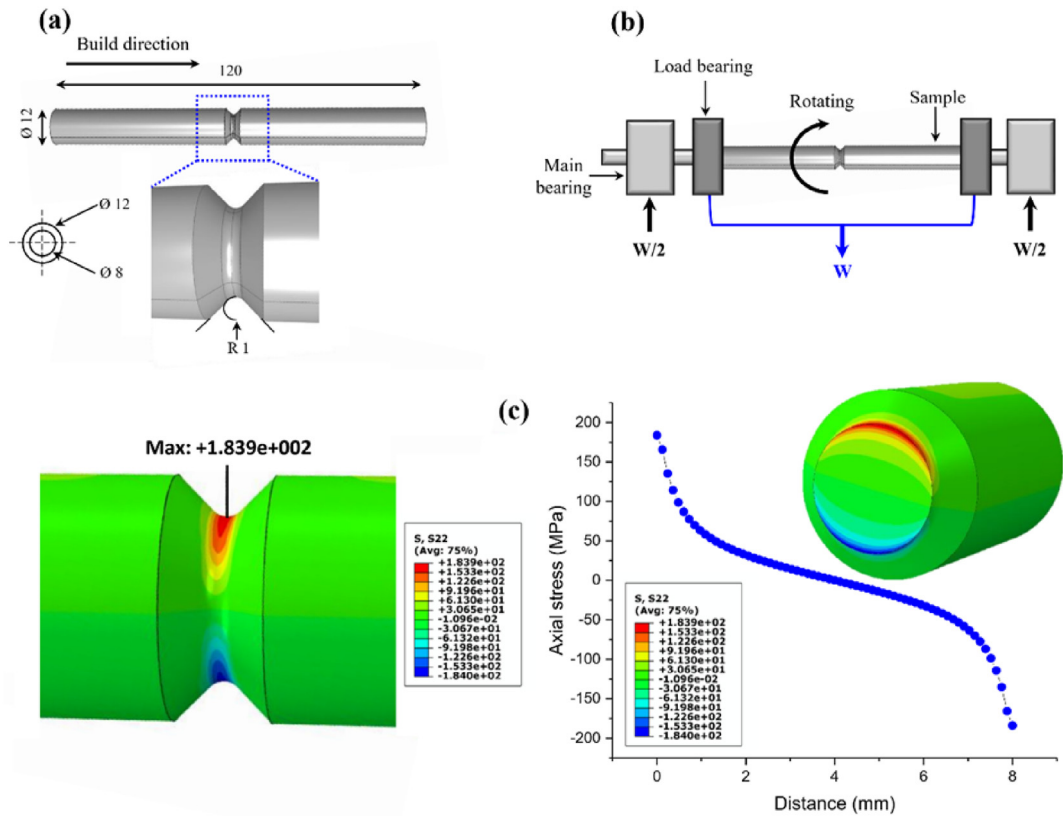

Fig. 3 − (a) Geometry of the cylindrical V-notched fatigue sample with notch root dimeter of R = 1 mm (b) schematic illustration of the test set-up for rotating bending fatigue test (c) FE stress contour and distribution of axial stresses in the sample's cross section under the applied load.

for continuous mapping of the experimental results of hardness and residual stresses along the minimum cross-section. Afterwards, two different network architectures were constructed for analyzing the correlation between various parameters. All ML-based models were developed using MATLAB R2021a software.

Fig. 4a schematically presents the induced CRS after applying a peening treatment. By careful controlling of the effective parameters, peening treatments can induce a uniform distribution of CRS on the treated surface [55]. Corresponding homogenous distribution of induced CRS is shown in Fig. 4b in a 2D contour. Fig. 4c indicates symmetrical cross-sectional mapping of the CRS distribution on the cylindrical part.

Generally, in the samples subjected to peening-based treatments, the crack initiation site is displaced from the surface to the sub-surface layers, mainly due to the generation of deep CRS and surface work hardening [56,57]. To evaluate the effect of the applied treatments in inducing sub-surface crack initiation rather than surface cracks, the corresponding hardness and residual stress values induced by each treatment were mapped continuously on the fracture surfaces of the failed samples. For instance, Fig. 5a depicts the scanning electron microscopy (SEM) micrograph of fracture surface of AB + LSP2 sample at different magnifications of ×50, × 100 and × 250 from left to the right, respectively. The sub-surface crack initiation site can be clearly identified at the highest used magnification. The same magnification was also used for identifying the sub-surface initiation site in the samples treated by SP and SVP, as shown in the result's section.

On the fracture surface with magnification of × 250, an area with maximum width of 480 μm in the central bottom part and length of 800 μm was considered (see Fig. 5b). This area was meshed using radial coordinate (r, θ). To obtain a continuous 2D contour that can cover the whole considered area, a SNN with a structure of 2 + 10+5 + 1, rate of training of 0.195, and hidden and output layer transfer functions of Logsig was developed. The r, θ coordinates of each measurement point in the meshed area were considered as the inputs of the network and the corresponding hardness and residual stresses values were regarded as the output parameters. The measured values of hardness and residual stresses were firstly assigned to point with $\theta = 0°$ at different corresponding r values (considering their distance from the surface) and then assigned to the rest of

the points with θ ranging from −90 to 90°. Then, continuous distributions were predicted at different depths, where experimental measurements were not performed to cover the whole meshed area. For example, Fig. 5c presents the mapped CRS distribution of AB + LSP2 sample in the considered area. It should be noted similar SNN (with a structure of 2 + 10+5 + 1, rate of training of 0.195, and hidden and output layer transfer functions of Logsig) was used for prediction of residual stresses and microhardness distributions of all sets of samples for continuous mapping on the corresponding fracture surface planes. Comparison of the predicted and experimental values of residual stresses and microhardness obtained by the developed SNNs is shown in Fig. A (in Appendix A).

To describe the parameters considered for developing the ML-based models, the fracture surface of all sets of samples and the related surface and mechanical properties were analyzed carefully. As an example, the distance of the crack initiation site from the free surface is measured for AB + LSP2 sample to be around 155 μm (Fig. 6a). The schematic illustration of the considered area that describes the analyzed parameters of crack initiation depth (d), corresponding values of hardness (H_d), the corresponding residual stress (S_d) values at crack initiation site as well as the applied stress during fatigue test at that point (S_f), is presented in Fig. 6b. Each sample was also characterized with its individual surface roughness (R_a), number of fatigue life cycles before failure (N_f) and core hardness (H_c). H_d and S_d values were extracted from the continuous mapping of hardness and residual stress by ML, whereas R_a, N_f and H_c parameters were directly obtained from the experiments. In addition, the values of S_f at different depths from surface were estimated by FE simulation (see Fig. 3d). The total stress at the crack initiation site was estimated by superimposing the corresponding residual stress and the applied stress at that depth i.e ($S_d + S_f$).

As confirmed in our previous studies on fatigue assessment of notched LPBF parts [53,58], despite the high stress concentration at the notch root (as shown in Fig. 3c), the fatigue fracture in these parts did not necessarily occur on the notch root plane. Interestingly, in most cases the fracture initiated in an offset plane with respect to the notch root plane, in the downward face area; this was mainly attributed to the considerably higher surface roughness in the downface area (as illustrated in Fig. 1b) [59]. As shown in Fig. 6c, relative
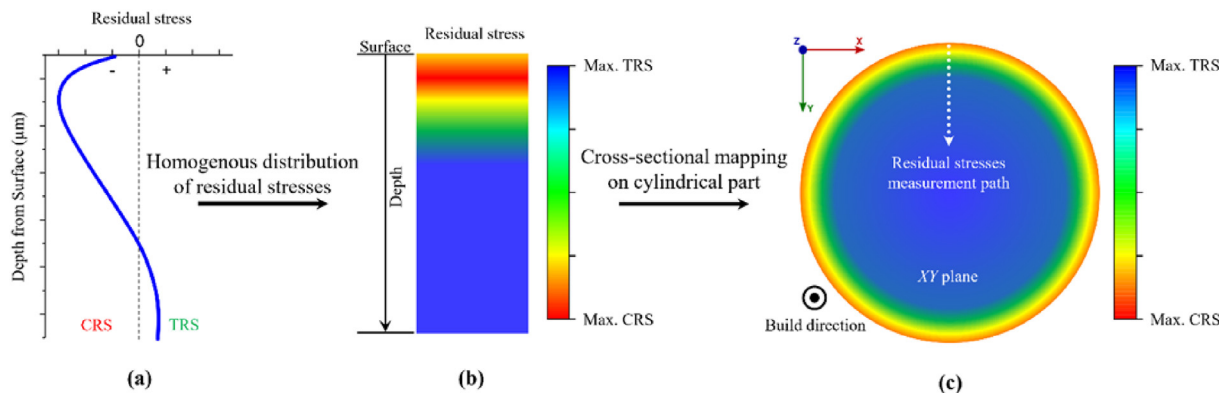

Fig. 4 − Schematic illustration of (a) the induced CRS after applying a peening treatment (b) the corresponding homogenous distribution of CRS in a 2D contour and (c) cross-sectional symmetric mapping of the CRS distribution on sample's cross section.
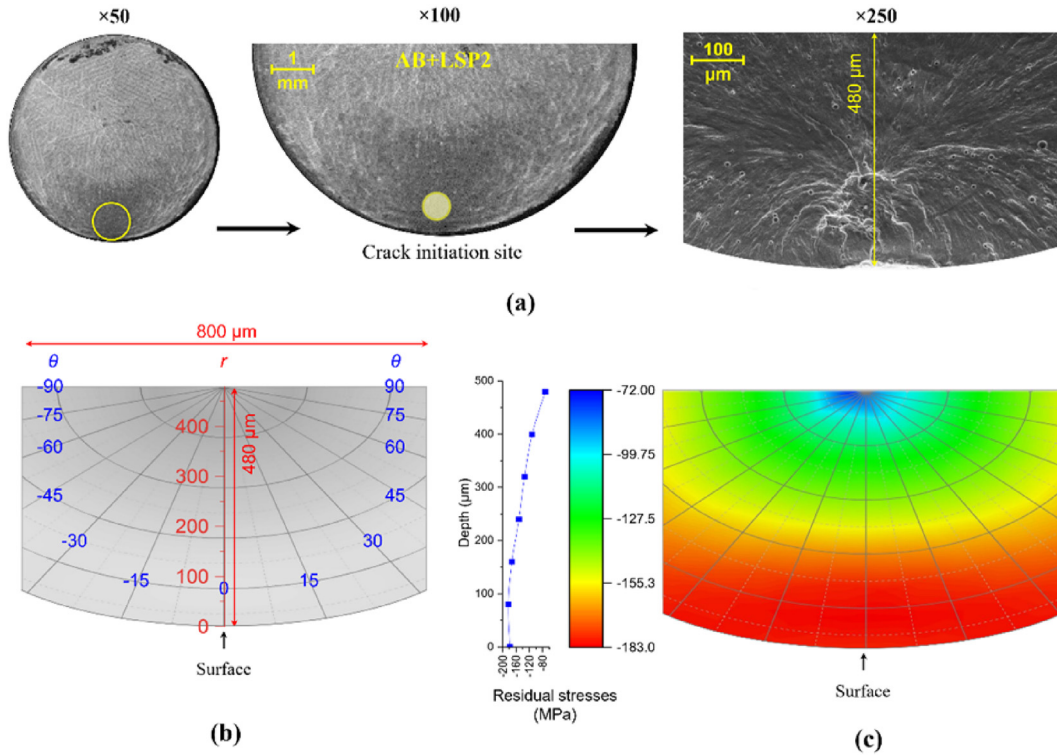
Fig. 5 − (a) SEM micrographs of fracture surface for AB + LSP2 sample with different magnifications (b) considered area with a maximum width of 480 μm in the centre and a length of 800 μm meshed using radial coordinate (r, θ). (c) continuous mapping of the corresponding CRS distribution (before fatigue loading) in AB + LSP2 sample in the considered area.

height of fracture plane parameter (h/h_0), which is defined as the ratio of the distance of the fracture plane (h) to the total notch opening distance (h_0) was used to describe the fracture plane displacement from the notch root section.

Considering all the aforementioned parameters, in this study two different ML-based models based on deep learning approach were developed. In Model A, as shown in Fig. 7a, the parameters of $S_d + S_f$, H_d/H_c (used as an index of hardening) and R_a were considered as inputs and parameters of d, h/h_0 and N_f were regarded as outputs. In this way, the correlation between hardness, residual and amplitude stresses as well as

surface roughness was estimated with crack initiation sites. This model can also analyze the effects of hardening and CRS as well as roughness variation caused by the peening-based treatments on fatigue behavior of the notched LPBF AlSi10Mg samples. On the other hand, in Model B, as presented in Fig. 7b, the parameters of d and h/h_0 were considered as inputs and N_f was gathered as output parameter to specify the effects of crack initiation site on fatigue life of the treated samples. Different NN approaches including SNN, DNN and SADNN were developed to find the optimum structure with the best performance for each model. In all the developed
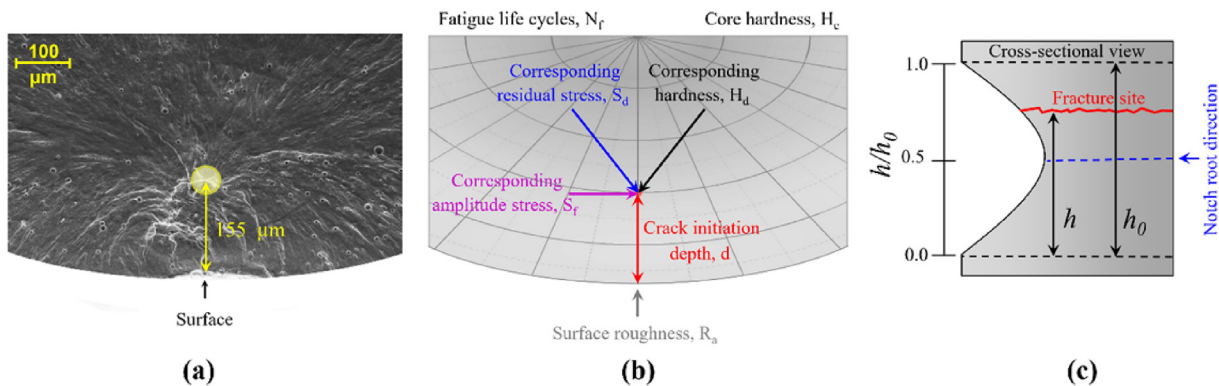

Fig. 6 − (a) Measuring the depth of sub-surface crack initiation site for AB + LSP2 sample (b) schematic illustration of the considered area on the fracture plane with the analyzed parameters of crack initiation depth (d), its corresponding hardness value (H_d), residual stress (S_d) and applied stress (S_f) with individual surface roughness (R_a), fatigue life cycle (N_f) and core hardness (H_c) for the specimen (c) schematic description of relative height (h/h_0) of fracture plane.
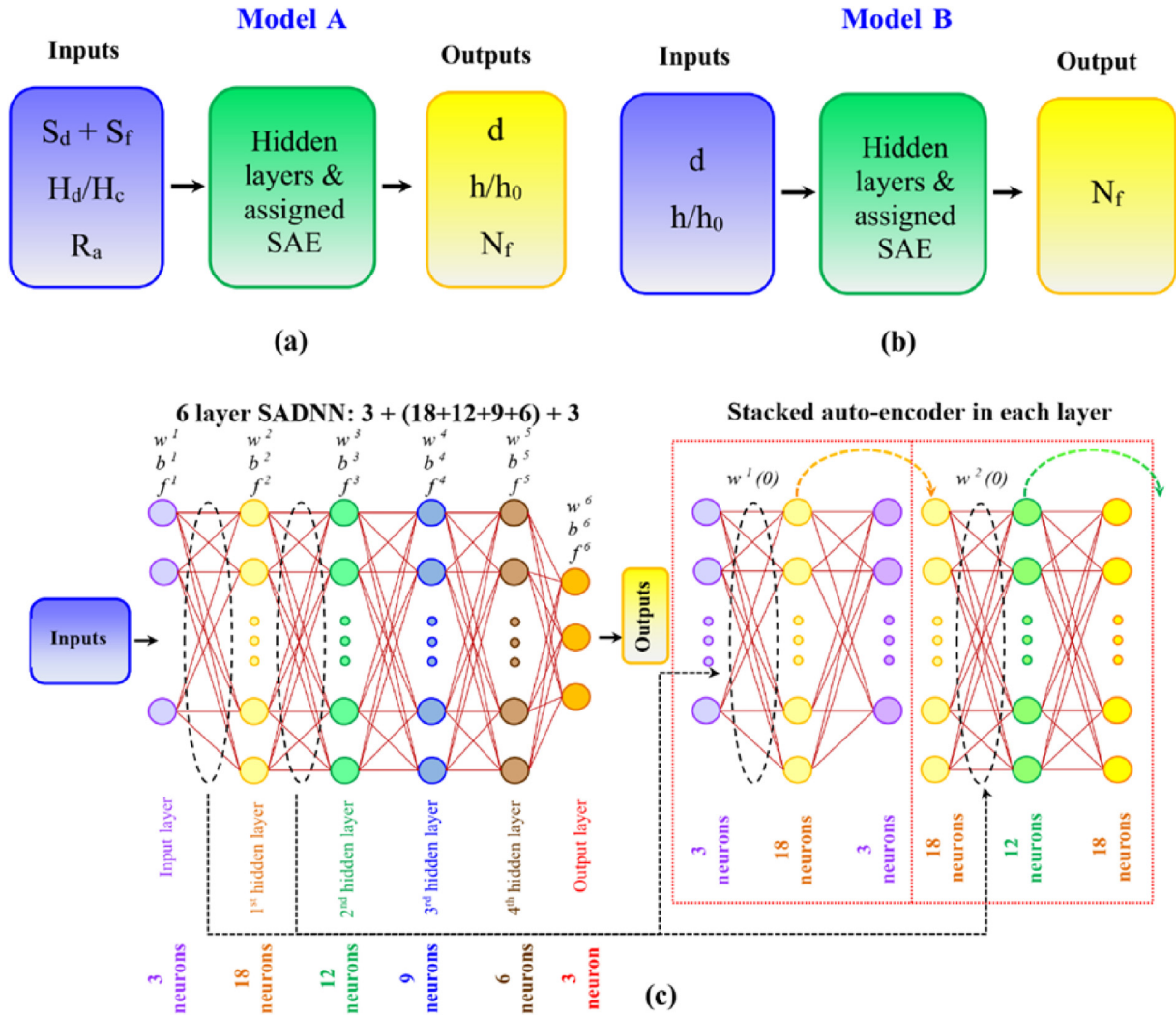
Fig. 7 – The considered input and output parameters in the developed ML-based networks of (a) Model A and (b) Model B (c) schematic illustration of a SADNN with 6 layers and structure of 3+(18 + 12+9 + 6)+3 used for Model A.

networks, random data selection strategy was followed for training and testing processes and the data used for training was not employed in testing step. The performance of the developed networks was examined in terms of accuracy using correlation coefficient (R^2) calculated as follows [60]:

$$R^2 = \frac{\sum\limits_{i=1}^{n}\left(f_{EXP,i} - F_{EXP}\right)\left(f_{ANN,i} - F_{ANN}\right)}{\sqrt{\sum\limits_{i=1}^{n}\left(\left(f_{EXP,i} - F_{EXP}\right)^2\left(f_{ANN,i} - F_{ANN}\right)^2\right)}} \quad (1)$$

where, n is the number of the fed data to the network, and f_{EXP} and f_{ANN} represent the experimental and predicted values, respectively, determined as follows:

$$F_{EXP} = \frac{1}{n}\sum_{i=1}^{n}f_{EXP,i} \quad (2.a)$$

$$F_{ANN} = \frac{1}{n}\sum_{i=1}^{n}f_{ANN,i} \quad (2.b)$$

Fig. 7c depicts the schematic illustration of a 6 layer DNN (with 4 hidden layers) and the assigned SAE with an architecture of 3+(18 + 12+9 + 6)+3 layers used for Model A. SAE was assigned in between the layers of DNN for pre-training of the fed experimental data. Based on the size of the dataset and also the complexity of the modeled phenomena, a DNN should be developed with or without pre-training [61]. As the used dataset for feeding is relatively small in this work, we took advantage of the potentials of SAEs. Generally, for constructing a fully inter-connected SADNN with y layers, y-1 SAEs are required. In the developed SADNN with 6 layers consisting of input layer +4 hidden layers + output layer, 5 SAEs were used considering the same number of neurons in each SAE with the corresponding DNN layer. Hence with respect to the number of layers and neurons, in the 6 layers SADNN, SAEs with 3+(18)+3, 18+(12)+18, 12+(9)+12, 9+(6)+9, 6+(3)+6 architectures were assigned. Detailed description of SAE development and performance were reported in different studies [62–64].

After performance assessment of the developed NNs for specifying the optimum structures with the highest accuracy, the model function of the selected NN was generated for further parametric and sensitivity analyses. The corresponding model function of the developed SADNN can be obtained as follows:

$$a^1 = f^1\left(w^1\,i + b^1\right) \tag{3}$$

$$a^2 = f^2(w^2 i^1 + b^2) \tag{4}$$

$$a^3 = f^3\left(w^3 i^2 + b^3\right) \tag{5}$$

$$a^4 = f^4\left(w^4 i^3 + b^4\right) \tag{6}$$

$$a^5 = f^5\left(w^5 i^4 + b^5\right) \tag{7}$$

where I_j is the importance of the jth input parameter relevant to the output parameter, N_i and N_h are the numbers of input and hidden neurons, respectively, and W is the connection weight; the superscripts i, h, and o, in turn, refer to input, hidden and output neurons.

4.   Results and discussions

4.1.   Experimental results

Fig. 8a represents the confocal top-surface morphological observations in the notch root area of the AB and surface treated samples. The surface irregularities of the as-built state such as spatters and partially and unmelted powders were mostly removed after applying peening-based treatments of SP, SVP and LSP. The formation of dimples and overlaps in the

$$a^6 = M(m(1), m(2), m(3)) = f^6\left(w^6 i^5 + b^6\right) = f^6\left(w^6 f^5\left(w^5 f^4\left(w^4 f^3\left(w^3 f^2\left(w^2 f^1\left(w^1 i + b^1\right) + b^2 + b^3\right) + b^4\right) + b^5\right) + b^6\right)\right) \tag{8}$$

where a^1, a^2, a^3, a^4 and a^5 are the outputs of the first to fifth layers, respectively and the function M assigns the values of the considered 3 inputs of $S_d + S_f$, H_d/H_c and R_a to the outputs of d, h/h_0 and N_f with $m(1)$, $m(2)$ and $m(3)$, respectively. Moreover, a sensitivity analysis was carried out to specify the importance of each input parameter on the variations of outputs considering the weight matrix of the developed SADNN and Garson equation, as follows [65]:

$$\frac{\sum_{m=1}^{N_h}\left(\left(\frac{\left|W_{jm}^{ih}\right|}{\sum_{k=1}^{N_i}\left|W_{km}^{ih}\right|}\right) \times \left|W_{mn}^{ho}\right|\right)}{\sum_{k=1}^{N_i}\left\{\sum_{m=1}^{N_h}\left(\frac{\left|W_{km}^{ih}\right|}{\sum_{k=1}^{N_i}\left|W_{km}^{ih}\right|}\right) \times \left|W_{mn}^{ho}\right|\right\}} \tag{9}$$

peened samples with shots (SP and SVP) due to multiple impacts and surface-to-surface contacts with the peening media can be seen. However, in the LSP treated sample, lower surface roughness scatter was observed with very few local surface imperfections. Surface roughness measured in terms of arithmetic mean, R_a is presented in Fig. 8b. The results indicate that SVP had the highest effects on roughness reduction followed by LSP, while SP slightly increased the surface roughness.

Different mechanical properties including hardness and residual stresses as well as fatigue life of all sets of samples were analyzed. Microhardness measurement were performed on the longitudinal cross section (*YZ plane*) of the samples along notch root direction to assess the local influence of peening-based post-treatments as depicted in Fig. 9a up to the depth of 480 μm (as described in Fig. 5 according to considered
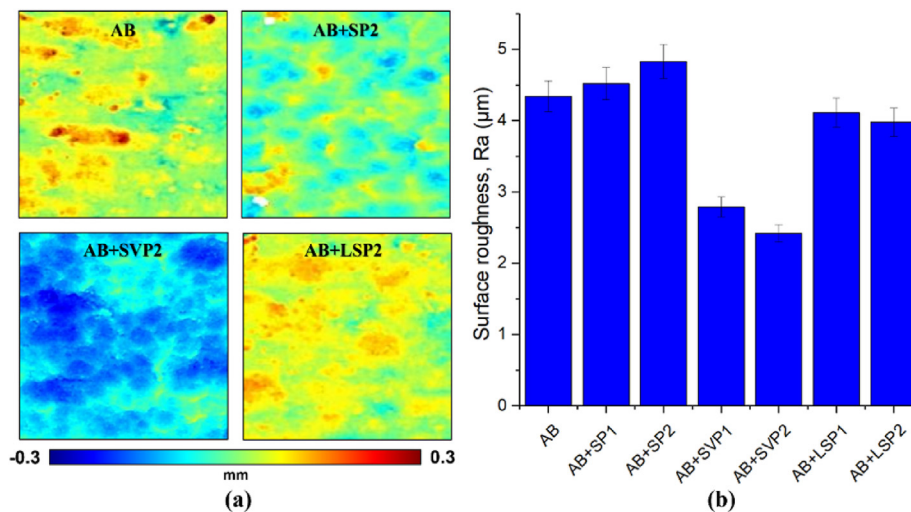

Fig. 8 — (a) Confocal microscopy observations of the notch root surface of the AB, AB + SP2, AB + SVP2 and AB + LSP2 samples (b) measured values of surface roughness in terms of R_a.
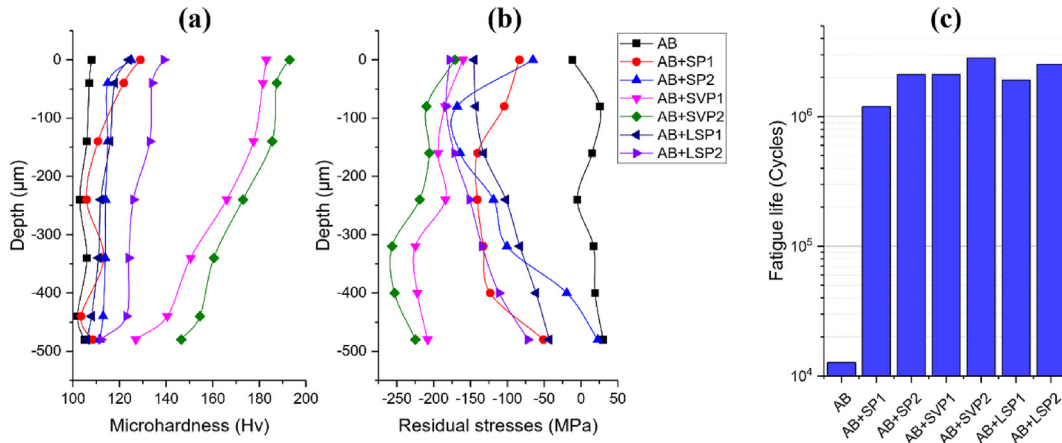
Fig. 9 – (a) Microhardness profiles in the notch root section of samples and (b) residual stress distributions in all sets of samples measured from top surface through the depth (c) number of cycles to failure for rotating bending fatigue tests considering a fixed amplitude stress of 110 MPa.

area in fracrture surface). The microhardness in the surface layer of the peened samples gradually decreased through interior. The applied processes with higher energy had more efficiency for in-depth hardening of the notch root. Surface hardness improvements of 19, 15, 69, 78, 14 and 28% were obtained for AB + SP1, AB + SP2, AB + SVP1, AB + SVP2, AB + LSP1 and AB + LSP2 samples, respectively.

Residual stresses distributions from top surface were measured for all sets of samples using XRD as depicted in Fig. 9b. AB sample showed tensile residual stresses, while the peened samples exhibited significant CRSs. Surface CRSs of −83, −65, −160, −170, −145 and −178 MPa were achieved for AB + SP1, AB + SP2, AB + SVP1, AB + SVP2, AB + LSP1 and AB + LSP2 samples, respectively. Considering the applied stress distribution by fatigue loading (which obtained by FE analysis) up to the depth of 480 μm and the measured residual stresses in all sets of samples, the stress superposition under cyclic loading can be determined by calculating the sum of the

stresses as presented in Fig. B(in Appendix B). In addition, 2D contours of superposed stresses in all sets considering homogeneous distribution of stresses are presented in Fig. C(in Appendix C).

Fatigue lives of all sets of V-notched LPBF AlSi10Mg samples under a stress amplitude of 110 MPa were obtained as represented in Fig. 9c. The results revealed remarkable fatigue life improvement after applying peening-based post-treatments. Fatigue life of AB sample with 1.26×10^4 cycles was increased up to 1.19×10^6, 1.75×10^6, 2.12×10^6, 2.83×10^6, 1.92×10^6 and 2.53×10^6 cycles in the AB + SP1, AB + SP2, AB + SVP1, AB + SVP2, AB + LSP1 and AB + LSP2 samples, respectively. Fracture surface of the samples were analyzed, and the location of the crack initiation sites were identified. Fig. 10a, reveals the depths of crack initiation sites for all sets of samples measured for 5 samples per each set. The cracks were initiated from the surface in the case of AB samples; however, in all the peened samples sub-surface
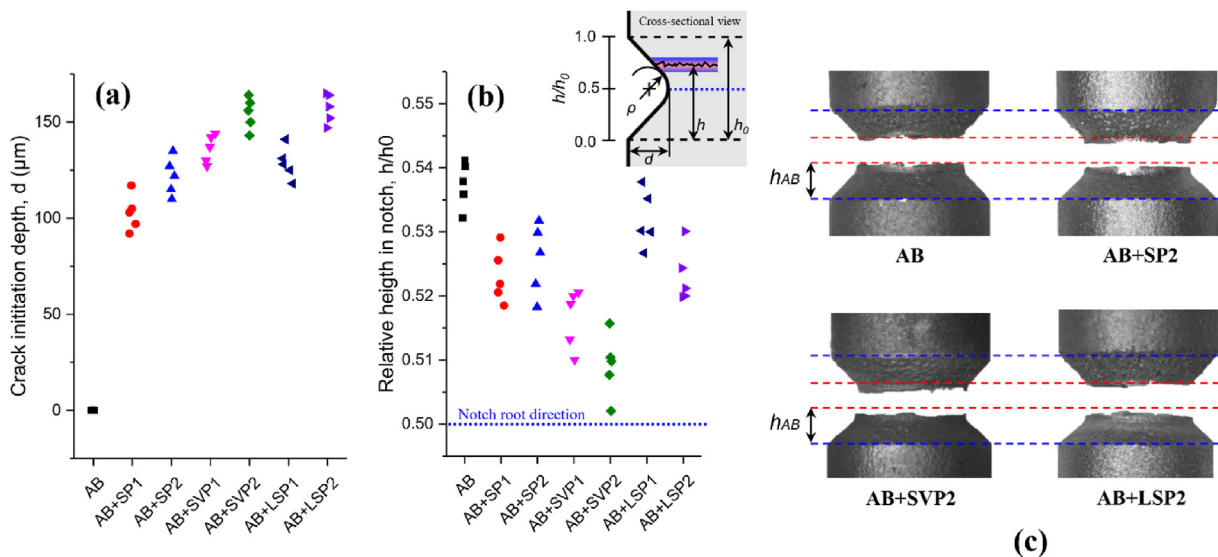

Fig. 10 – (a) Crack initiation depths and (b) the measured relative heights of fracture plane for all sets of samples (c) the displacement of the fracture planes in the AB + SP2, AB + SVP2 and AB + LSP2 samples compared to the AB sample.
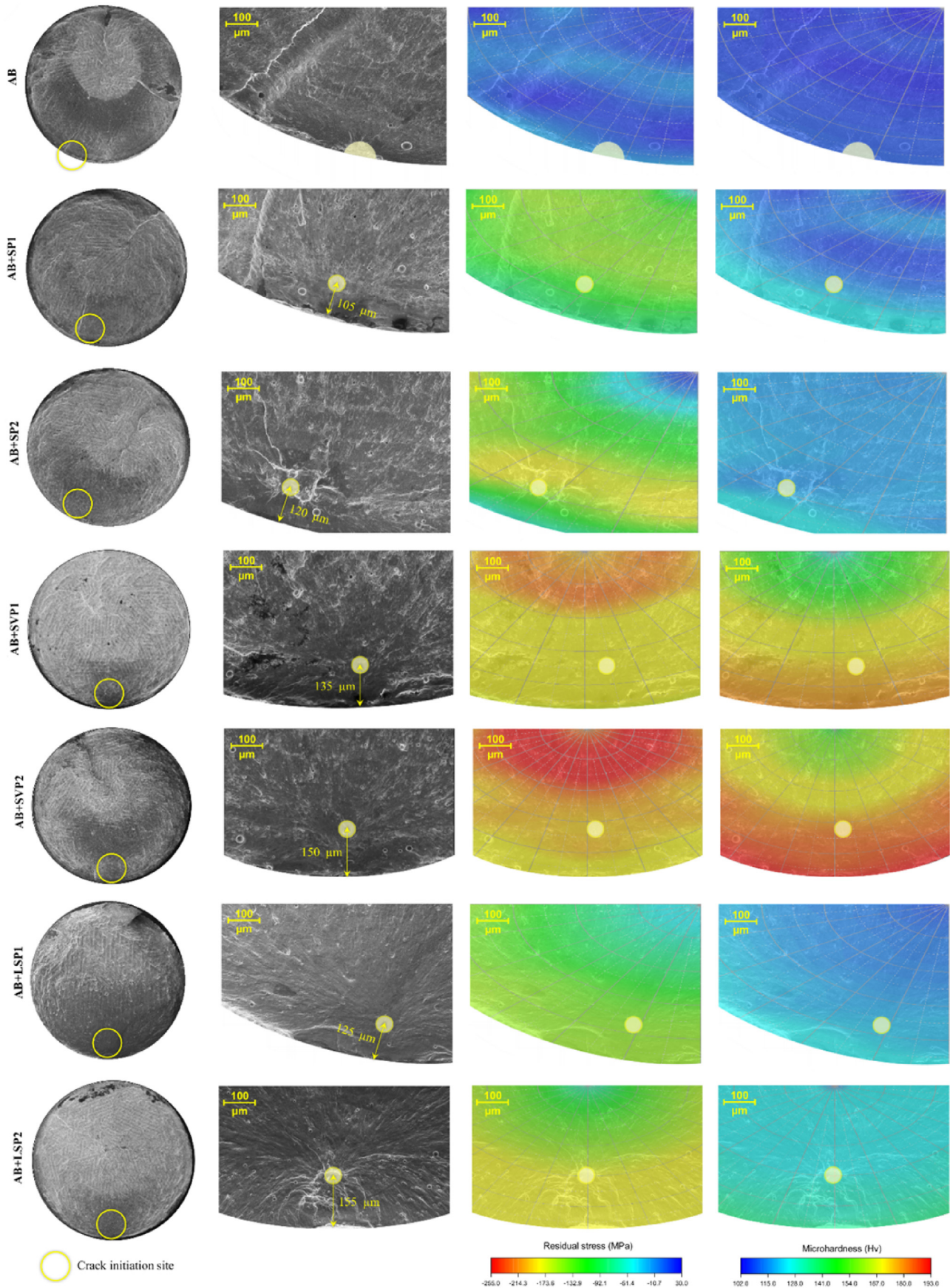
Fig. 11 — Crack initiation sites in all sets of samples with mapped residual stress (corresponding to the XRD measurements made before fatigue loading) and hardness on the area around it on the fracture surface.

Table 2 — The obtained values related to input and output parameters considering the samples presented in Fig. 11

Sample	S_d (MPa)	S_f (MPa)	$S_d + S_f$ (MPa)	H_d (Hv)	H_d/H_c	R_a (μm)	d (μm)	$h/h0$	N_f (Cycles)
AB	−11	183.9	172.9	108	1.02	4.34	0	0.5431	12,690
AB + SP1	−136	167.5	31.5	118	1.11	4.52	105	0.5291	1,196,470
AB + SP2	−171	165.2	−5.8	115	1.09	4.83	115	0.5182	2,119,660
AB + SVP1	−183	163.1	−19.9	176	1.66	2.79	130	0.5132	2,121,670
AB + SVP2	−191	156.8	−34.2	184	1.74	2.42	150	0.5098	2,832,250
AB + LSP1	−149	164.9	15.9	118	1.11	4.11	125	0.5352	1,921,670
AB + LSP2	−175	153.8	−21.2	131	1.24	3.98	165	0.5243	2,530,250

crack initiations were observed. In addition, considering the fracture planes of the broken samples, the relative heights of fracture site were calculated as shown in Fig. 10b. The results indicated that all the applied surface post-treatments had considerable effects on reduction of relative height of fracture plane and relocating the fracture planes closer to the notch root section. Fig. 10c illustrates the displacement of the fracture planes in the AB + SP2, AB + SVP2 and AB + LSP2 samples, respectively compared to the AB sample.

4.2. Modelling results

Fig. 11 presents the fracture surfaces of all sets of samples specifying the crack initiation sites and mapping of the residual stresses and hardness on the corresponding fracture plane. Sub-surface crack initiation can be observed clearly for all peened samples (shown with yellow circle).

Table 3 — The accuracy of the selected SADNNS in both training and testing processes for Model A and Model B.

Model	SADNN structure	Output	R^2	
			Training	Testing
A	3+(18 + 12+9 + 6)+3	d	0.961	0.950
		h/h_0	0.974	0.968
		N_f	0.965	0.957
B	2+(18 + 12+9 + 6)+1	N_f	0.985	0.972

For correlating the mechanical properties with fatigue crack initiation site and fatigue life, for instance for the samples presented in Fig. 11, the considered input and output parameters (mentioned in Fig. 7a) are summarized in Table 2. It should be mentioned that H_c of 105.5, which was obtained from the average of the measured microhardnesses for AB sample was considered for the determination of H_d/H_c. The
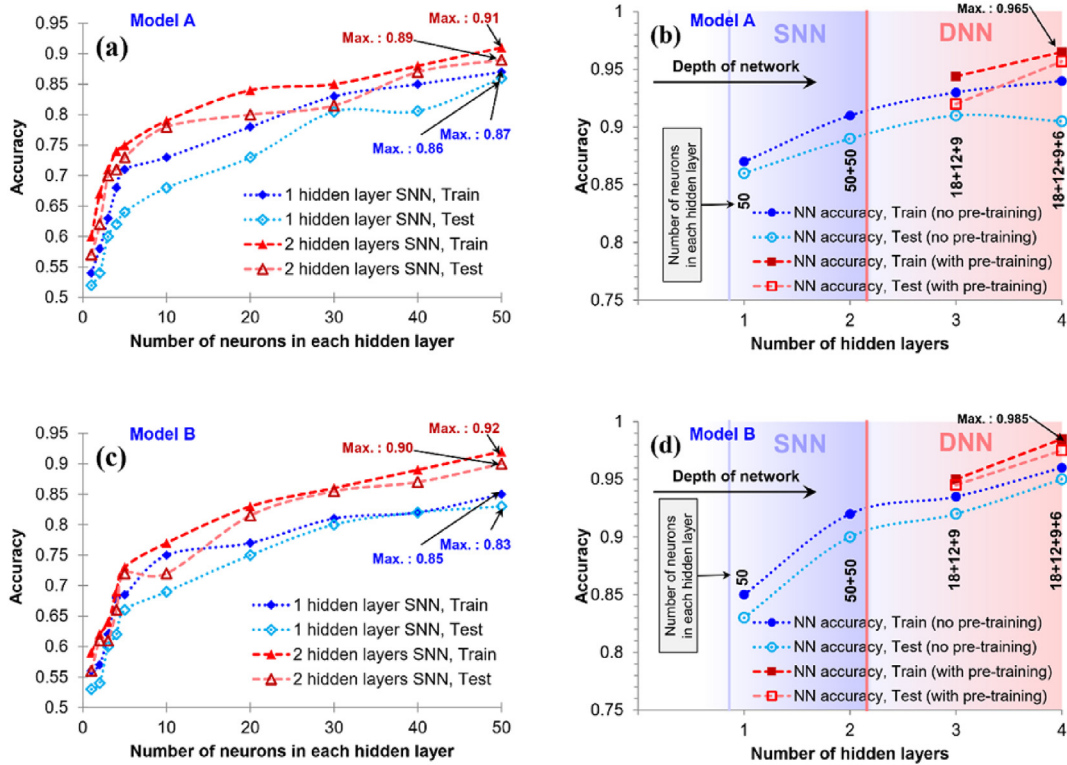

Fig. 12 — (a,c) The effects of number of neurons in each layer of SNNs with 1 and 2 hidden layers on the accuracy of the estimated fatigue life for models A and B. (b,d) Comparison of the accuracy of the estimated fatigue life obtained by SNNs, DNNs and SADNNs for models A and B.

same procedure was followed for the other 4 samples analyzed for the same set and finally a data set with 35 data points were obtained and used for the training process.

The average values of each input parameter were used for testing the developed networks. Different NNs including SNN, DNN and SADNN were developed and their efficiencies in terms of prediction accuracy were compared as presented in Fig. 12. It should be mentioned that these results are presented in terms of accuracy of output parameter of fatigue life in both Model A and Model B. In all the constructed NNs, network parameters of 0.165 for training rate and the Logarithmic-Sigmod (logsig) transfer functions in hidden and output layers were used. Dealing with the developed SNNs with 1 and 2 hidden layers, by raising the number of neurons in each layer as well as increasing the number of layers, the accuracy of the predicted results increased as well (see Fig. 12a and c). In the developed SNNs, the networks with (50 + 50) hidden layers with accuracy of 0.91 and 0.92 (for training) had the best performance for Model A and Model B, respectively.

Comparison of the accuracy of the predicted fatigue life obtained by SNNs, DNNs and SADNNs in Model A and Model B is shown in Fig. 12a and b. The results indicate that SADNNs

with a structures of 3+(18 + 12+9 + 6)+3 and 2+(18 + 12 +9 + 6)+1 exhibited the highest efficiencies in terms of accuracy compared to all the developed NNs with accuracies of 0.965 and 0.985 for Model A and Model B, respectively. After pre-training of the data via SAE, the performance of NNs was enhanced reaching to acceptable R^2. For example, considering the DNN developed with 4 hidden layers in Model A, the accuracy of the predicted results increased form 0.94 up to 0.965 after implementing pre-training by SAE. The performance assessment of the selected SADNNs, which had the highest accuracy in both training and testing processes, is shown in Table 3. All the selected SADNNs had accuracies higher than 0.95 for both training and testing processes. Fig. 13 shows the comparative diagrams of predicted values versus experimentally measured data for the considered output parameters in Models A and B.

To obtain the correlation between residual stress, hardness and surface roughness with crack initiation site and fatigue life of notched LPBF AlSi10Mg samples subjected to different peening treatments, parametric analyses were carried out. The corresponding model functions to the selected SADNNs were generated and the intervals of experimnetal data for all input parameters were used to achieve continious 2D
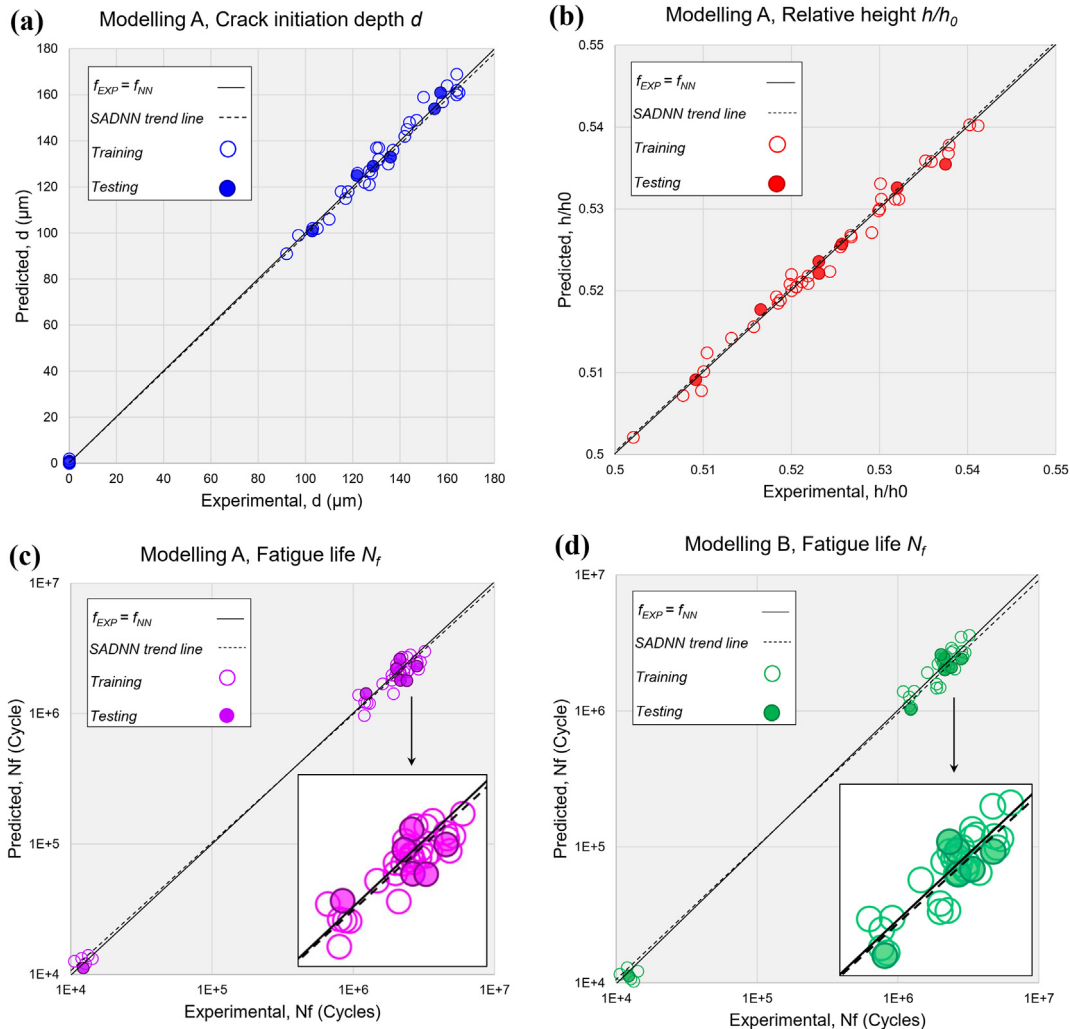

Fig. 13 — Comparative diagrams of the predicted and experimental results in terms of (a) *d*, (b) *h/h₀* (c,d) N_f.

contours. Fig. 14 illustrates the results of paramertric analyses of Model A in terms of d, h/h_0 and N_f.

As shown in Figs. 14a−c it can be seen that by decreasing $S_d + S_f$ and R_a while increasing H_d/H_c (which can be obtained by applying peening treatments) the depth of crack initiation site d increased. Dealing with the relative height of fracture plane, as presented in Fig. 14d−f, reducing $S_d + S_f$ and R_a and increasing H_d/H_c, led to reduction in h/h_0 values. In addition, as illustrated in Fig. 14g−i, fatigue life N_f, improved by reducing $S_d + S_f$ and R_a and increasing H_d/H_c. Overall, the results
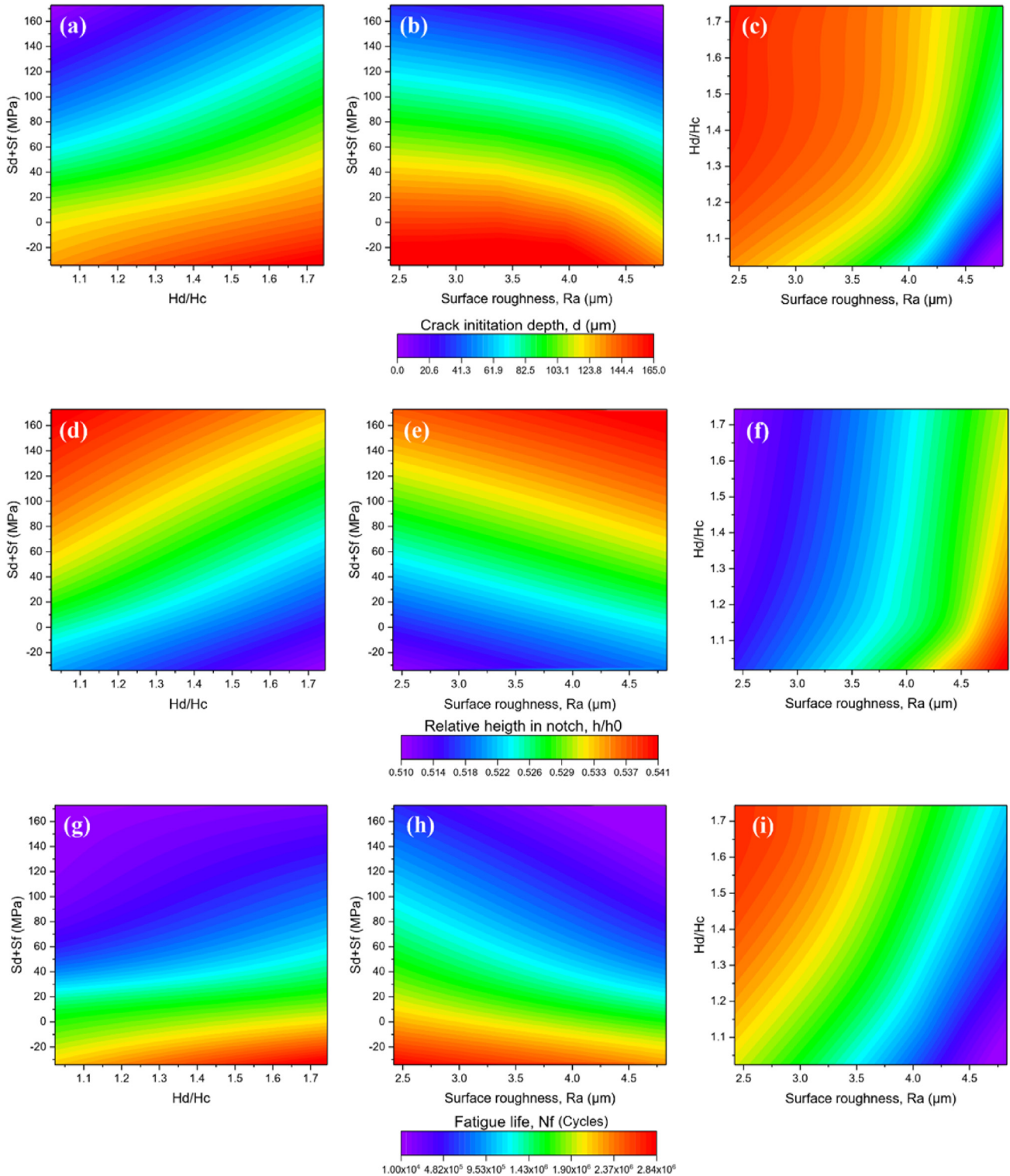

Fig. 14 − 2D contours presenting the parametric analyses results for Model A in terms of (a) S_d;+ S_f and H_d/H_c, (b) S_d;+ S_f and R_a and (c) R_a and H_d/H_c versus d (d) $S_d + S_f$ and H_d/H_c, (e) $S_d + S_f$ and R_a and (f) R_a and H_d/H_c versus h/h_0; (g) $S_d + S_f$ and H_d/H_c, (h) $S_d + S_f$ and R_a and (i) R_a and H_d/H_c versus N_f.
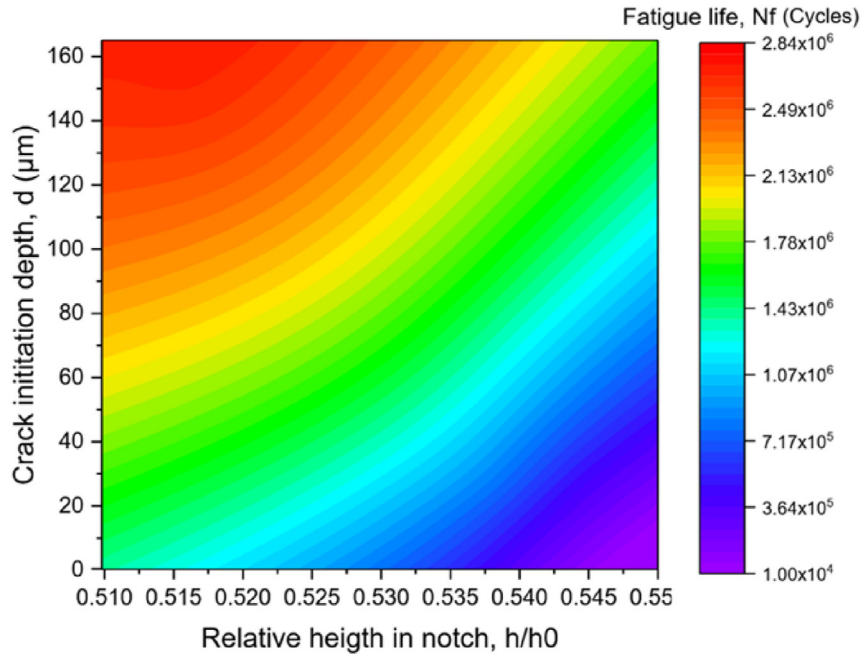
Fig. 15 – 2D contour presenting the parametric analysis result for Model B in terms of *d* and *h/h₀* versus *N_f*.

indicate that by increasing the hardening, inducing higher CRSs and more surface roughness reduction, higher crack initiation depth, lower relative height of fracture plane and higher fatigue life can be expected.

The results of parametric analysis for Model B are presented in Fig. 15. A direct relation was observed for the depth of sub-surface crack initiation site with fatigue life improvement. d was considerably increased by inducing higher CRSs, hardening and roughness reduction as results of peening treatments, thus leading to longer fatigue life. In addition, by displacing the relative height of fracture plane from downwards face of the notch with poor surface quality closer to the notch root section (that theoretically has the highest stress consternation) and therefore reduction of h/h_0 by applying post-treatments, fatigue life can be significantly improved. Hence, all the parametric analyses confirmed the beneficial

effects of the peening-based post-processing methods for fatigue life improvement.

To specify the effects of each considered input data on the variations of output parameters, sensitivity analyses were performed. Fig. 16a and b presents the results of sensitivity analyses for Models A and B, respectively. Considering Model A, the results indicate that parameter of $S_d + S_f$, incorporating the effects of both induced residual and applied stresses, had the highest effect on the variations of output parameters including d, h/h_0 and N_f followed by surface roughness R_a and hardening index of H_d/H_c. The considered input parameters exhibited different levels of importance with respect to different outputs. For instance, R_a had an importance of 21% on the variation of output parameter of d, while in the case of output parameter of h/h_0 higher importance of 39% was estimated. Dealing with Model B, which had only one output parameter, crack initiation
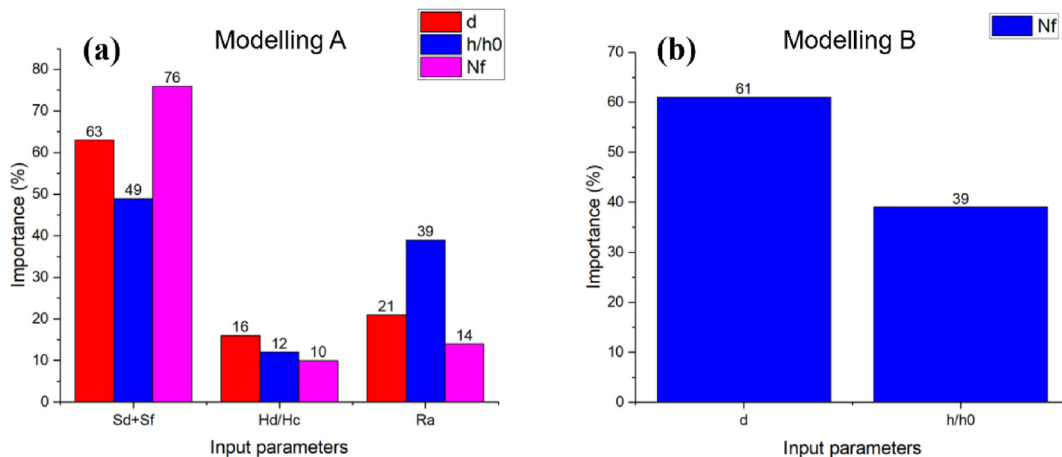

Fig. 16 – Sensitivity analyses results for (a) Model A and (b) Model B.

depth d had higher effects on fatigue life improvement compared to the relative height of fracture plane.

5.   Conclusions

In this study, experimental data, numerical models and deep learning approaches were implemented to correlate residual stress, hardness and surface roughness with the depth of crack initiation site and fatigue behavior of V-notched LPBF AlSi10Mg samples subjected to different peening treatments. According to the results the following conclusions can be drawn.

- All the applied peening-based surface treatments including SP, SVP and LSP induced considerable CRSs, surface layer hardening, surface morphology modification and roughness reduction. The combined effect of the affected properties resulted in significant fatigue life improvement.
- Considering post-treatments with higher energy, SVP had the highest effects on fatigue life improvement with 223 times higher fatigue life compared to the as-built set, followed by LSP (× 199 times) and SP (× 94 times).
- Fractography analysis of the failed samples after rotating bending fatigue tests revealed sub-surface crack initiation in all samples but at different depths. However, in the as-built state, the poor surface quality led to surface crack initiation. In addition, the surface post-treatments considerably reduced the relative height of fracture plane, shifting it towards the notch root plane.
- Performance evaluation of the developed neural network models showed that by pre-training of the small dataset, it

is possible to get acceptable accuracies in the predictions up to more than 0.96 (out of 1 as maximum R^2).
- Correlations between residual stress, hardness, and surface roughness with the depth of crack initiation site and fatigue life, obtained via parametric analyses revealed that by increasing surface layer hardening and inducing higher CRSs, besides surface roughness reduction, deeper crack initiation site, lower relative height of fracture plane and superior fatigue life can be obtained.
- As one of the major findings of this study, it was found that the depth of sub-surface crack initiation had direct relation with fatigue life improvement. Likewise, by displacing the relative height of the fracture plane closer to the notch root section by applying surface post-treatments, higher fatigue lives were obtained.
- The results of sensitivity analyses indicated that the combination of residual and applied stresses had the highest effect on the variation of crack initiation depth, the relative height of the fracture plane and fatigue life followed by surface roughness and hardening index, respectively.

Declaration of Competing Interest

The authors declare that they have no known competing financial interests or personal relationships that could have appeared to influence the work reported in this paper.
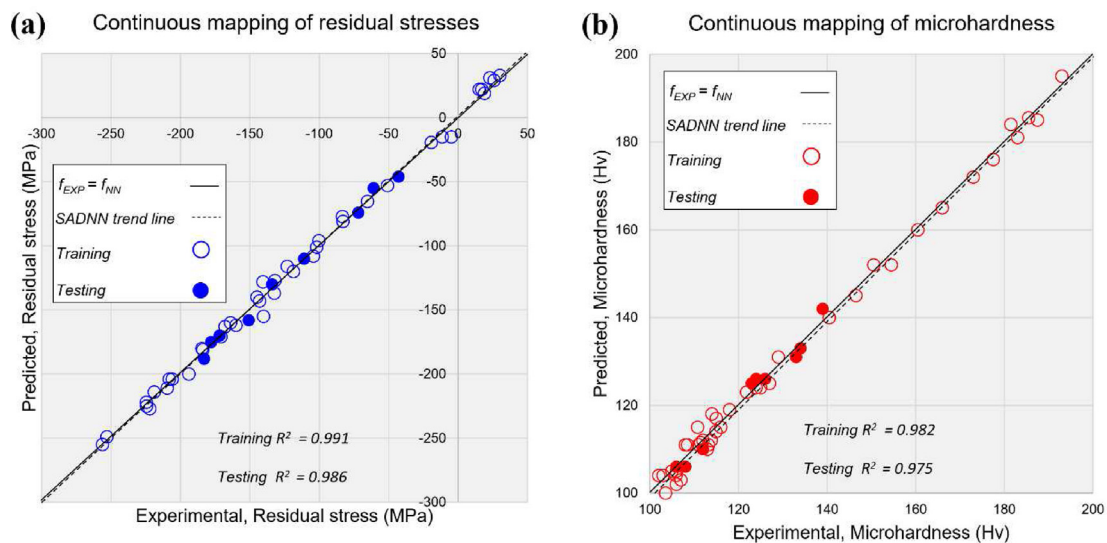
Appendix A

Fig. A − Comparison of the predicted and experimental values of residual stresses and microhardness obtained by the developed SNNs.
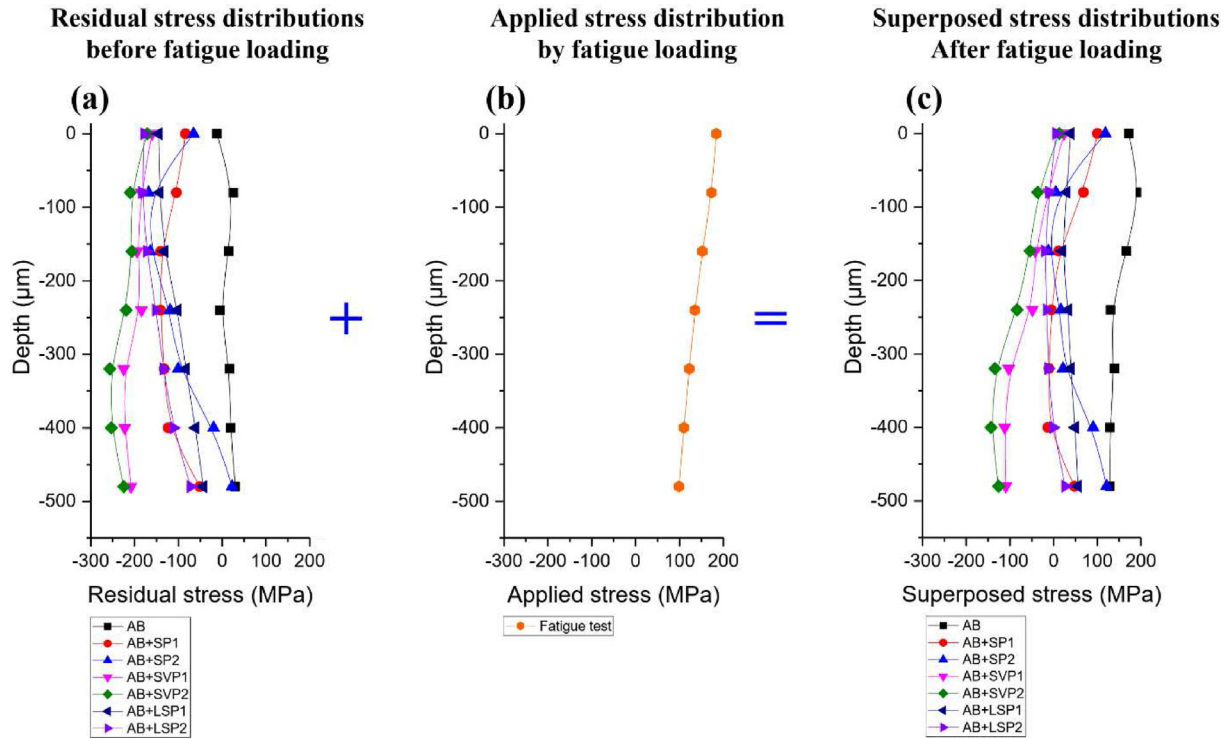
Appendix B

Fig. B − Distributions of (a) residual stresses before fatigue loading, (b) applied stress by fatigue loading and (c) superposed stresses after fatigue loading.
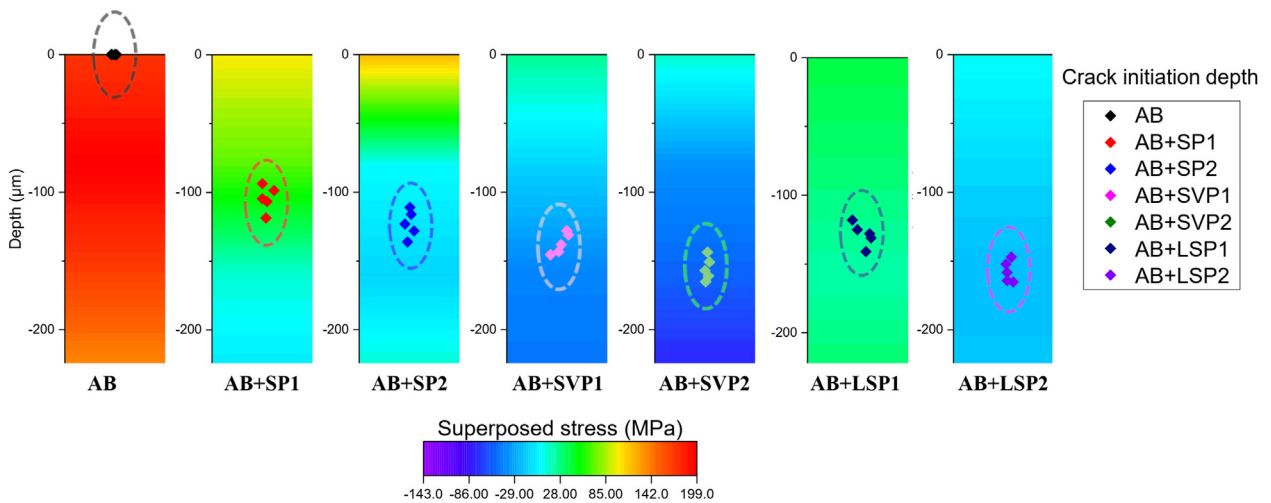
Appendix C

Fig. C − 2D contours of superposed stresses in all sets considering homogeneous distribution of stresses and the crack initiation depths.

REFERENCES

[1] Herzog D, Seyda V, Wycisk E, Emmelmann C. Additive manufacturing of metals. Acta Mater 2016;117:371—92. https://doi.org/10.1016/j.actamat.2016.07.019.

[2] Ferro P, Fabrizi A, Berto F, Savio G, Meneghello R, Rosso S. Defects as a root cause of fatigue weakening of additively manufactured AlSi10Mg components. Theor Appl Fract Mech 2020;108:102611. https://doi.org/10.1016/j.tafmec.2020.102611.

[3] Aboulkhair NT, Everitt NM, Ashcroft I, Tuck C. Reducing porosity in AlSi10Mg parts processed by selective laser melting. Addit Manuf 2014;1:77—86. https://doi.org/10.1016/j.addma.2014.08.001.

[4] Mfusi BJ, Mathe NR, Tshabalala LC, Popoola PAI. The effect of stress relief on the mechanical and fatigue properties of additively manufactured AlSi10Mg parts. Metals 2019;9. https://doi.org/10.3390/met9111216.

[5] Mukherjee T, Zhang W, DebRoy T. An improved prediction of residual stresses and distortion in additive manufacturing. Comput Mater Sci 2017;126:360—72. https://doi.org/10.1016/j.commatsci.2016.10.003.

[6] Sames WJ, List FA, Pannala S, Dehoff RR, Babu SS. The metallurgy and processing science of metal additive manufacturing. Int Mater Rev 2016;61:315—60. https://doi.org/10.1080/09506608.2015.1116649.

[7] Zhang Z, Sun C, Xu X, Liu L. Surface quality and forming characteristics of thin-wall aluminium alloy parts manufactured by laser assisted MIG arc additive manufacturing. Int J Light Mater Manuf 2018;1:89—95. https://doi.org/10.1016/j.ijlmm.2018.03.005.

[8] Li R, Liu J, Shi Y, Wang L, Jiang W. Balling behavior of stainless steel and nickel powder during selective laser melting process. Int J Adv Manuf Technol 2012;59:1025—35. https://doi.org/10.1007/s00170-011-3566-1.

[9] Maleki E, Bagherifard S, Bandini M, Guagliano M. Surface post-treatments for metal additive manufacturing: progress, challenges, and opportunities. Addit Manuf 2021;37:101619. https://doi.org/10.1016/j.addma.2020.101619.

[10] Nasab MH, Gastaldi D, Lecis NF, Vedani M. On morphological surface features of the parts printed by selective laser melting (SLM). Addit Manuf 2018;24:373—7. https://doi.org/10.1016/j.addma.2018.10.011.

[11] Xu Z, Liu A, Wang X. Fatigue performance and crack propagation behavior of selective laser melted AlSi10Mg in 0°, 15°, 45° and 90° building directions. Mater Sci Eng, A 2021;812. https://doi.org/10.1016/j.msea.2021.141141.

[12] Beretta S, Gargourimotlagh M, Foletti S, du Plessis A, Riccio M. Fatigue strength assessment of "as built" AlSi10Mg manufactured by SLM with different build orientations. Int J Fatig 2020;139. https://doi.org/10.1016/j.ijfatigue.2020.105737.

[13] Maleki E, Bagherifard S, Unal O, Sabouri F, Bandini M, Guagliano M. Effects of different mechanical and chemical surface post-treatments on mechanical and surface properties of as-built laser powder bed fusion AlSi10Mg. Surf Coating Technol 2022;439:128391. https://doi.org/10.1016/j.surfcoat.2022.128391.

[14] Salvati E, Lunt AJG, Ying S, Sui T, Zhang HJ, Heason C, et al. Eigenstrain reconstruction of residual strains in an additively manufactured and shot peened nickel superalloy compressor blade. Comput Methods Appl Mech Eng 2017;320:335—51. https://doi.org/10.1016/j.cma.2017.03.005.

[15] Lesyk DA, Dzhemelinskyi VV, Martinez S, Mordyuk BN, Lamikiz A. Surface shot peening post-processing of inconel 718 alloy parts printed by laser powder bed fusion additive manufacturing. J Mater Eng Perform 2021;30:6982—95. https://doi.org/10.1007/s11665-021-06103-6.

[16] Alharbi N. Corrosion resistance of 3D printed SS316L post-processed by ultrasonic shot peening at optimum energy level. 2022. https://doi.org/10.1177/09544054221112164.

[17] Maleki E, Bagherifard S, Unal O, Bandini M, Guagliano M. The effects of microstructural and chemical surface gradients on fatigue performance of laser powder bed fusion AlSi10Mg. Mater Sci Eng, A 2022;840:142962. https://doi.org/10.1016/j.msea.2022.142962.

[18] Soyama H, Okura Y. The use of various peening methods to improve the fatigue strength of titanium alloy Ti6Al4V manufactured by electron beam melting. AIMS Mater Sci 2018;5:1000—15. https://doi.org/10.3934/MATERSCI.2018.5.1000.

[19] Sato M, Takakuwa O, Nakai M, Niinomi M, Takeo F, Soyama H. Using cavitation peening to improve the fatigue life of titanium alloy Ti-6Al-4V manufactured by electron beam melting. Mater Sci Appl 2016;7:181—91. https://doi.org/10.4236/msa.2016.74018.

[20] Xing X, Duan X, Jiang T, Wang J, Jiang F. Ultrasonic peening treatment used to improve stress corrosion resistance of AlSi10Mg components fabricated using selective laser melting. Metals 2019;9. https://doi.org/10.3390/met9010103.

[21] Du Plessis A, Glaser D, Moller H, Mathe N, Tshabalala L, Mfusi B, et al. Pore closure effect of laser shock peening of additively manufactured AlSi10Mg. 3D Print Addit Manuf 2019;6:245—52. https://doi.org/10.1089/3dp.2019.0064.

[22] Jinoop AN, Subbu SK, Paul CP, Palani IA. Post-processing of laser additive manufactured inconel 718 using laser shock peening. Int J Precis Eng Manuf 2019;20:1621—8. https://doi.org/10.1007/s12541-019-00147-4.

[23] Yeo I, Bae S, Amanov A, Jeong S. Effect of laser shock peening on properties of heat-treated Ti—6Al—4V manufactured by laser powder bed fusion. Int J Precis Eng Manuf - Green Technol 2021;8:1137—50. https://doi.org/10.1007/s40684-020-00234-2.

[24] Jiang Q, Li S, Zhou C, Zhang B, Zhang Y. Effects of laser shock peening on the ultra-high cycle fatigue performance of additively manufactured Ti6Al4V alloy. Opt Laser Technol 2021;144. https://doi.org/10.1016/j.optlastec.2021.107391.

[25] Lesyk DA, Martinez S, Mordyuk BN, Pedash OO, Dzhemelinskyi VV, Lamikiz A. Ultrasonic surface post-processing of hot isostatic pressed and heat treated superalloy parts manufactured by laser powder bed fusion. Addit Manuf Lett 2022;3:100063. https://doi.org/10.1016/j.addlet.2022.100063.

[26] Zhang H, Zhao J, Liu J, Qin H, Ren Z, Doll GL, et al. The effects of electrically-assisted ultrasonic nanocrystal surface modification on 3D-printed Ti-6Al-4V alloy. Addit Manuf 2018. https://doi.org/10.1016/j.addma.2018.04.035.

[27] Maleki E, Unal O, Bandini M, Guagliano M, Bagherifard S. Individual and synergistic effects of thermal and mechanical surface post-treatments on wear and corrosion behavior of laser powder bed fusion AlSi10Mg. J Mater Process Technol 2022;302:117479. https://doi.org/10.1016/j.jmatprotec.2021.117479.

[28] Efe Y, Karademir I, Husem F, Maleki E, Karimbaev R, Amanov A, et al. Enhancement in microstructural and mechanical performance of AA7075 aluminum alloy via severe shot peening and ultrasonic nanocrystal surface modification. Appl Surf Sci 2020;528. https://doi.org/10.1016/j.apsusc.2020.146922.

[29] Donoghue J, Antonysamy AA, Martina F, Colegrove PA, Williams SW, Prangnell PB. The effectiveness of combining rolling deformation with Wire-Arc Additive Manufacture on β-grain refinement and texture modification in Ti-6Al-4V. Mater Char 2016;114:103—14. https://doi.org/10.1016/j.matchar.2016.02.001.

[30] Amanov A. Effect of local treatment temperature of ultrasonic nanocrystalline surface modification on tribological behavior and corrosion resistance of stainless steel 316L produced by selective laser melting. Surf Coating Technol 2020;398. https://doi.org/10.1016/j.surfcoat.2020.126080.

[31] Maleki E, Bagherifard S, Sabouri F, Guagliano M. Effects of hybrid post-treatments on fatigue behaviour of notched LPBF AlSi10Mg: experimental and deep learning approaches. Procedia Struct Integr 2021;34:141–53. https://doi.org/10.1016/j.prostr.2021.12.021.

[32] Baek MS, Kreethi R, Park TH, Sohn Y, Lee KA. Influence of heat treatment on the high-cycle fatigue properties and fatigue damage mechanism of selective laser melted AlSi10Mg alloy. Mater Sci Eng, A 2021. https://doi.org/10.1016/j.msea.2021.141486.

[33] Aboulkhair NT, Maskery I, Tuck C, Ashcroft I, Everitt NM. Improving the fatigue behaviour of a selectively laser melted aluminium alloy: influence of heat treatment and surface quality. Mater Des 2016. https://doi.org/10.1016/j.matdes.2016.05.041.

[34] Raja A, Cheethirala SR, Gupta P, Vasa NJ, Jayaganthan R, Clement CD, et al. A review on the fatigue behaviour of AlSi10Mg alloy fabricated using laser powder bed fusion technique. J Manuf Mater Process 2022;106568:6. https://doi.org/10.1016/j.jmrt.2022.01.028.

[35] Clement CD, Masson J, Kabir AS. Effects of heat treatment on microstructure and mechanical properties of AlSi10Mg fabricated by selective laser melting process. J Manuf Mater Process 2022;6. https://doi.org/10.3390/jmmp6030052.

[36] Maleki E, Unal O. Shot peening process effects on metallurgical and mechanical properties of 316 L steel via: experimental and neural network modeling. Met Mater Int 2021;27:262–76. https://doi.org/10.1007/s12540-019-00448-3.

[37] Maleki E, Unal O, Reza Kashyzadeh K. Fatigue behavior prediction and analysis of shot peened mild carbon steels. Int J Fatigue 2018;116:48–67. https://doi.org/10.1016/j.ijfatigue.2018.06.004.

[38] Khatir S, Tiachacht S, Le Thanh C, Ghandourah E, Mirjalili S, Abdel Wahab M. An improved Artificial Neural Network using Arithmetic Optimization Algorithm for damage assessment in FGM composite plates. Compos Struct 2021. https://doi.org/10.1016/j.compstruct.2021.114287.

[39] Wang S, Wang H, Zhou Y, Liu J, Dai P, Du X, et al. Automatic laser profile recognition and fast tracking for structured light measurement using deep learning and template matching. Meas J Int Meas Confed 2021. https://doi.org/10.1016/j.measurement.2020.108362.

[40] Ho LV, Trinh TT, De Roeck G, Bui-Tien T, Nguyen-Ngoc L, Abdel Wahab M. An efficient stochastic-based coupled model for damage identification in plate structures. Eng Fail Anal 2022. https://doi.org/10.1016/j.engfailanal.2021.105866.

[41] Ho LV, Nguyen DH, Mousavi M, De Roeck G, Bui-Tien T, Gandomi AH, et al. A hybrid computational intelligence approach for structural damage detection using marine predator algorithm and feedforward neural networks. Comput Struct 2021. https://doi.org/10.1016/j.compstruc.2021.106568.

[42] Hinton GE, Osindero S, Teh YW. A fast learning algorithm for deep belief nets. Neural Comput 2006;18:1527–54. https://doi.org/10.1162/neco.2006.18.7.1527.

[43] Hinton GE, Salakhutdinov RR. Reducing the dimensionality of data with neural networks. 80- Science 2006;313:504–7. https://doi.org/10.1126/science.1127647.

[44] Bengio Y, Lamblin P, Popovici D, Larochelle H. Greedy layer-wise training of deep networks. Adv Neural Inf Process Syst 2007:153–60. https://doi.org/10.7551/mitpress/7503.003.0024.

[45] Feng S, Zhou H, Dong H. Using deep neural network with small dataset to predict material defects. Mater Des 2019;162:300–10. https://doi.org/10.1016/j.matdes.2018.11.060.

[46] Liu G, Bao H, Han B. A stacked autoencoder-based deep neural network for achieving gearbox fault diagnosis. Math Probl Eng 2018;2018. https://doi.org/10.1155/2018/5105709.

[47] Wang Y Bin, You ZH, Li X, Jiang TH, Chen X, Zhou X, et al. Predicting protein-protein interactions from protein sequences by a stacked sparse autoencoder deep neural network. Mol Biosyst 2017;13:1336–44. https://doi.org/10.1039/c7mb00188f.

[48] Maleki E, Bagherifard S, Razavi SMJ, Bandini M, du Plessis A, Berto F, et al. On the efficiency of machine learning for fatigue assessment of post-processed additively manufactured AlSi10Mg. Int J Fatigue 2022;160:106841. https://doi.org/10.1016/j.ijfatigue.2022.106841.

[49] Li J, Yang Z, Qian G, Berto F. Machine learning based very-high-cycle fatigue life prediction of Ti-6Al-4V alloy fabricated by selective laser melting. Int J Fatigue 2022. https://doi.org/10.1016/j.ijfatigue.2022.106764.

[50] Elangeswaran C, Cutolo A, Gallas S, Dinh TD, Lammens N, Erdelyi H, et al. Predicting fatigue life of metal LPBF components by combining a large fatigue database for different sample conditions with novel simulation strategies. Addit Manuf 2022. https://doi.org/10.1016/j.addma.2021.102570.

[51] Wang H, Li B, Xuan FZ. Fatigue-life prediction of additively manufactured metals by continuous damage mechanics (CDM)-informed machine learning with sensitive features. Int J Fatigue 2022;164. https://doi.org/10.1016/j.ijfatigue.2022.107147.

[52] Salvati E, Tognan A, Laurenti L, Pelegatti M, De Bona F. A defect-based physics-informed machine learning framework for fatigue finite life prediction in additive manufacturing. Mater Des 2022;222:111089. https://doi.org/10.1016/j.matdes.2022.111089.

[53] Maleki E, Bagherifard S, Razavi SMJ, Riccio M, Bandini M, du Plessis A, et al. Fatigue behaviour of notched laser powder bed fusion AlSi10Mg after thermal and mechanical surface post-processing. Mater Sci Eng, A 2022;829:142145. https://doi.org/10.1016/j.msea.2021.142145.

[54] Maleki E, Bagherifard S, Unal O, Bandini M, Guagliano M. On the effects of laser shock peening on fatigue behavior of V-notched AlSi10Mg manufactured by laser powder bed fusion. Int J Fatigue 2022;163:107035. https://doi.org/10.1016/j.ijfatigue.2022.107035.

[55] Maleki E, Farrahi GH, Reza Kashyzadeh K, Unal O, Gugaliano M, Bagherifard S. Effects of conventional and severe shot peening on residual stress and fatigue strength of steel AISI 1060 and residual stress relaxation due to fatigue loading: experimental and numerical simulation. Met Mater Int 2021;27:2575–91. https://doi.org/10.1007/s12540-020-00890-8.

[56] Benedetti M, Torresani E, Leoni M, Fontanari V, Bandini M, Pederzolli C, et al. The effect of post-sintering treatments on the fatigue and biological behavior of Ti-6Al-4V ELI parts made by selective laser melting. J Mech Behav Biomed Mater 2017;71:295–306. https://doi.org/10.1016/j.jmbbm.2017.03.024.

[57] Bagherifard S, Beretta N, Monti S, Riccio M, Bandini M, Guagliano M. On the fatigue strength enhancement of additive manufactured AlSi10Mg parts by mechanical and thermal post-processing. Mater Des 2018;145:28–41. https://doi.org/10.1016/j.matdes.2018.02.055.

[58] Maleki E, Bagherifard S, Sabouri F, Bandini M, Guagliano M. Hybrid thermal, mechanical and chemical surface post-treatments for improved fatigue behavior of laser powder

bed fusion AlSi10Mg notched samples. Surf Coating Technol 2022;430. https://doi.org/10.1016/j.surfcoat.2021.127962.

[59] Solberg K, Wan D, Berto F. Fatigue assessment of as-built and heat-treated Inconel 718 specimens produced by additive manufacturing including notch effects. Fatig Fract Eng Mater Struct 2020;43:2326—36. https://doi.org/10.1111/ffe.13300.

[60] Maleki E. Artificial neural networks application for modeling of friction stir welding effects on mechanical properties of 7075-T6 aluminum alloy. IOP Conf Ser Mater Sci Eng 2015;103. https://doi.org/10.1088/1757-899X/103/1/012034.

[61] Yamanaka A, Kamijyo R, Koenuma K, Watanabe I, Kuwabara T. Deep neural network approach to estimate biaxial stress-strain curves of sheet metals. Mater Des 2020;195. https://doi.org/10.1016/j.matdes.2020.108970.

[62] Maleki E, Unal O, Guagliano M, Bagherifard S. Analysing the fatigue behaviour and residual stress relaxation of gradient nano-structured 316L steel subjected to the shot peening via deep learning approach. Met Mater Int 2022;28:112—31. https://doi.org/10.1007/s12540-021-00995-8.

[63] Shao H, Xia M, Wan J, De Silva CW. Modified stacked autoencoder using adaptive morlet wavelet for intelligent fault diagnosis of rotating machinery. IEEE/ASME Trans Mechatronics 2022. https://doi.org/10.1109/TMECH.2021.3058061.

[64] Law A, Ghosh A. Multi-label classification using a cascade of stacked autoencoder and extreme learning machines. Neurocomputing 2019. https://doi.org/10.1016/j.neucom.2019.05.051.

[65] Olden JD, Joy MK, Death RG. An accurate comparison of methods for quantifying variable importance in artificial neural networks using simulated data. Ecol Model 2004;178:389—97. https://doi.org/10.1016/j.ecolmodel.2004.03.013.